RSC Advances

PAPER

View Article Online
View Journal | View Issue

Cite this: *RSC Adv.*, 2015, **5**, 36428

Highly efficient formaldehyde elimination over meso-structured M/CeO_2 (M = Pd, Pt, Au and Ag) catalyst under ambient conditions†

Gengnan Li and Liang Li*

Received 20th March 2015
Accepted 15th April 2015

DOI: 10.1039/c5ra04928h

www.rsc.org/advances

A series of mesoporous CeO_2 supported noble metal (Pt, Pd, Au and Ag) catalysts, fabricated through a facial pyrolysis and *in situ* reduction protocol, were used for formaldehyde elimination under ambient conditions. The materials possessed relatively high specific surface area and uniformly dispersed noble metal nanoparticles, and showed very high catalytic activities for formaldehyde oxidation. For about 1 wt% noble metal loaded materials, Pt/CeO_2, Pd/CeO_2 and Au/CeO_2 catalysts could completely catalytically oxidize HCHO at room temperature. Even for the low activity Ag/CeO_2 catalyst, the complete conversion temperature could reach 100 °C, much lower than that reported before. Such good catalytic properties could be attributed to the strong synergetic interaction between the active component and CeO_2 nano-crystalline aggregated support. The reaction mechanism over the noble-metal/CeO_2 catalyst was also discussed through *in situ* DRIFTS analysis.

1. Introduction

Formaldehyde, one of the most noxious indoor gaseous pollutants, is commonly emitted from decorative and building materials. Long-term exposure may cause serious problems to human health even under a few ppm concentration. Research for the complete elimination of formaldehyde is thus of great importance for both practical application and fundamental research.[1,2] Although various methods have been proposed so far to remove this kind of indoor pollutant, they all can be classified as the adsorption and the catalytic oxidation strategy.[3–18] In comparison, catalytic oxidation under ambient condition is much attractive way to remove formaldehyde, because this process could not only constantly convert formaldehyde to non-harmful carbon dioxide and water molecules with low consumption of energy, but also absolutely overcome the disadvantage of the limited removal capacities of absorbent during absorption process.[2,19]

Cerium oxide, especially its nano-crystalline, always possesses large amount of oxygen vacancies and thus shows excellent oxygen storage and release properties, which are also critical factors for oxidation process. When combined with noble metal, benefitting from the strong synergetic interaction, significantly enhanced activity could be achieved. It has been proved that CeO_2 supported noble-metal materials are the promising catalysts for many oxidation catalysis process, including the oxidation of formaldehyde.[7–9,20–25] Zhang *et al.* developed a three-dimensionally ordered macro-structured Au/CeO_2 catalyst, and the complete oxidation of HCHO could be obtained at 75 °C.[7] Zhu *et al.* found that Au/CeO_2 prepared by deposition–precipitation method could achieve complete HCHO conversion into CO_2 and H_2O at room temperature.[8] Ma *et al.* reported recently that Ag/CeO_2 nanosphere prepared by hydrothermal and impregnation method could completely eliminate HCHO above 110 °C under relatively high space velocity.[9] All above literatures clearly show that the catalytic activity of the CeO_2 supported noble metal catalyst is mainly related to the surface area, highly dispersed noble metal species and the existence form of the active component.

Herein, we present a simple and versatile protocol to prepare meso-structured noble metal/CeO_2 catalysts for formaldehyde elimination under ambient condition. Nano-crystalline intersectioned mesoporous CeO_2 support was directly pyrolysis from oxalate and noble metal nanoparticles was confined through *in situ* reduction. Compared with other method, this strategy is simple and time-saving. The resulting materials process high specific surface area and the noble nanoparticles could be highly deposited in/on the CeO_2 nano-crystalline support, and thus possess much high catalytic activities for formaldehyde oxidation.

2. Experimental

2.1 Materials preparation

10 mmol $Ce(NO_3)_3 \cdot 6H_2O$ was first dissolved into 100 ml aqueous solution, 30 ml 1 M oxalate was slowly added under

Key Laboratory for Ultrafine Materials of Ministry of Education, School of Materials Science and Engineering, East China University of Science and Technology, Meilong Road 130, Shanghai, China. E-mail: liliang@ecust.edu.cn

† Electronic supplementary information (ESI) available: The XRD patterns of $Ce_2(C_2O_4)_3 \cdot 2H_2O$ precursor, the XRD pattern and TEM image of CeO_2 support and the comparison of the catalyst performance over different noble-metal supported catalysts for formaldehyde oxidation reported previously. See DOI: 10.1039/c5ra04928h

vigorous stirring. The precipitate was filtered, washed with deionized water and dried at 60 °C. The mesoporous CeO_2 material was finally obtained after calcinated at 350 °C for 2 h.

A series of mesoporous CeO_2 supported noble mental catalysts were synthesized through an improved wet impregnation procedure. For Pd/CeO_2 catalyst, 0.5 g above synthesized mesoporous CeO_2 material was added in 25 ml aqueous solution containing calculated content of Na_2PdCl_4. After stirred for 2 h, 100 ml 0.1 M hydrazine hydrate was slowly added and stirred for 12 h successively. The resulting solid mass was collected through centrifugation, washed with water and dried at 60 °C for 24 h. The other noble metal/CeO_2 materials were synthesized similar with that of Pd/CeO_2.

2.2 Characterization

Powder X-ray diffraction (XRD) patterns were recorded on a Bruker D8 Focus powder diffract meter with graphite monochromatized Cu Kα radiation (λ = 0.15405 nm) operated at 40 kV. Nitrogen adsorption and desorption isotherms were measured on a Micromeritics ASAP 2020M analyzer at liquid nitrogen temperature (77 K). Prior to the measurements, the samples were degassed at 423 K in vacuum for 6 h. The specific surface area and pore size distribution were calculated using the Brunauer–Emmett–Teller (BET) and Barrett–Joyner–Halenda (BJH) methods, respectively. Transmission Electron Microscopy (TEM) observations were performed on a field emission JEM-2100 (JEOL) electron microscope operated at 300 kV equipped with a Gatan-666 electron energy loss spectrometer and energy dispersive X-ray spectrometer. XPS (X-ray photoelectron spectroscopy) signals were collected on a VG Micro MK II instrument using monochromatic Al Kα X-ray at 1486.6 eV operated at 200 W. All the elemental binding energies were referenced to the C (1s) line situated at 284.6 eV. Infrared spectra were recorded by a FTIR spectrometer (Nicolet iS10) equipped with a MCT detector. The sample cell was fitted with ZnSe windows. The sample was exposed to the corresponding reaction stream (60 ml min^{-1}). The DRIFT spectra obtained at 25 °C with a solution of 4 cm^{-1} and 50 scans. Typical gas mixture was 600 ppm HCHO, 20.0 vol% O_2 balanced with N_2.

2.3 Catalytic properties

The oxidation of HCHO was performed in a quartz tubular (i.d. = 6 mm) fixed-bed reactor under atmospheric pressure. 50 mg of catalyst was loaded in the rector and the reaction temperature was monitored by a thermo-couple placed in the middle of the catalyst bed. A gas mixture containing 600 ppm HCHO and 20.0 vol% O_2 balanced by N_2 was introduced as reactants. Gaseous HCHO was generated by following air through formalin in a saturator kept at 0 °C. The HCHO was analyzed by an online GC equipped with a FID detector. The gaseous products passed through a methanization converter filled with Ni catalyst and all the carbon-containing products were converted to methane before they went to the FID detector to ensure a high intensity of signal. In a typical runs, the reaction data were obtained after HCHO was performed for 30 min to achieve steady state. The HCHO conversion was calculated as follows:

$$\text{HCHO conversion } (\%) = \frac{[\text{HCHO}]_{\text{in}} - [\text{HCHO}]_{\text{out}}}{[\text{HCHO}]_{\text{in}}} \times 100\%$$

where $[HCHO]_{in}$ and $[HCHO]_{out}$ represent the HCHO concentration in inlet and outlet gas, respectively.

3. Results and discussion

3.1 Catalytic oxidation performance of different noble-metal/CeO_2 catalysts

Fig. 1 depicts the catalytic activities of HCHO oxidation over different noble metal/CeO_2 catalysts. It clearly shows that the as prepared Pd, Pt and Au loaded CeO_2 catalysts all process much higher catalytic activity for HCHO oxidation at ambient temperature. Under 600 ppm HCHO concentration and the gas hourly space velocities (GHSV) of 120 000 h^{-1}, all the HCHO could be complete eliminated over Pt/CeO_2 catalyst even the reaction temperature as lower as 20 °C. Comparatively, although the Pd/CeO_2 and Au/CeO_2 catalysts show a slight decreased catalytic activities, the HCHO still can be totally converted below the temperature of 22 °C and 28 °C, respectively. Even for the traditional lower-active Ag catalyst, the as prepared Ag/CeO_2 material could complete oxidize HCHO at 100 °C and 95% HCHO conversion could be achieved at 60 °C, much lower than reported before.[9] Meanwhile, to understand the intrinsically catalytic properties, the turn over frequency (TOF) of the catalysts were calculated and showed the much higher values for HCHO oxidation process when compared with related research results (ESI†).

Besides, the effect of GHSV to HCHO conversion over different catalysts are also presented in Fig. 1. For the highest active catalyst Pt/CeO_2 material, even the GHSV increase to

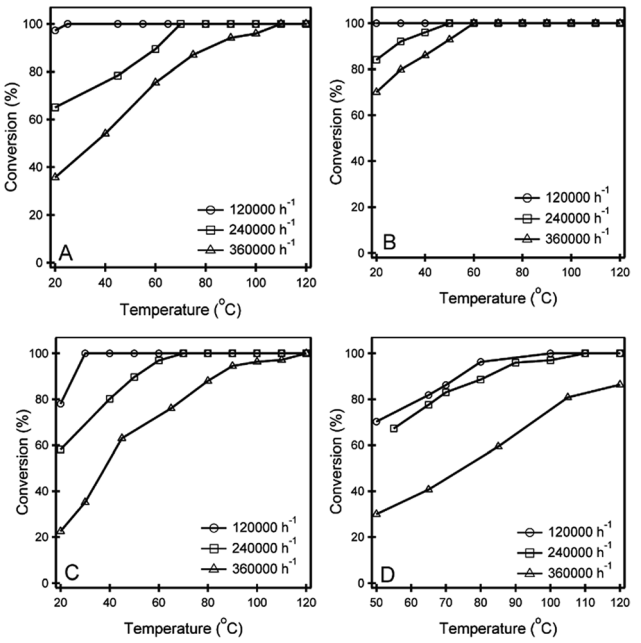

Fig. 1 Catalytic oxidation of HCHO over different noble metal/CeO_2 catalysts: Pd/CeO_2 (A), Pt/CeO_2 (B), Au/CeO_2 (C) and Ag/CeO_2 (D).

360 000 h^{-1}, HCHO still can be totally converted at the temperature of 60 °C and 70% conversion could be achieved at 20 °C. All these results appear that the noble-mental/CeO_2 catalysts prepared through pyrolysis and *in situ* reduction protocol are all among the most active catalysts reported in the literatures (ESI†).

3.2 Physicochemical properties of the catalysts

Highly dispersed noble metal species and high specific surface area CeO_2 support with large amount of oxygen vacancies are two key factors of highly active noble-metal/CeO_2 catalyst for HCHO oxidation under ambient conditions. In the experiment, the nano-crystalline inter-sectioned mesoporous CeO_2 support was obtained through direct pyrolysis of oxalate, and the noble metal component was transferred into the porous structure through wet impregnation and *in situ* reduction strategy. The actual contents of Pd, Pt, Au and Ag loaded in the meso-structured CeO_2 materials were determined by the ICP-AES technique to be 0.78, 1.00, 0.92 and 0.98 wt%, respectively. The result shows that almost all of the noble metal species in the aqueous solution have been deposited into/on the meso-structured CeO_2 support.

The crystalline structure of resulting noble-metal/CeO_2 materials were characterized by X-ray diffraction (XRD) analysis. After calcination, the precursor oxalate lost its original crystalline structure and turned to CeO_2 (PDF card no. 81-0792). No additional diffraction peaks from impurities were detected. Sequential impregnation and *in situ* reduction process did not affect the crystalline structure of the CeO_2 support. Fig. 2 presents the XRD patterns of the obtained noble metal/CeO_2 catalysts with different noble mental of Pd, Pt, Au and Ag, respectively. For Pd/CeO_2 and Pt/CeO_2 materials, except that for CeO_2 support, there is not any additional diffraction peaks for metallic Pd or Pt. This may be attribute to the small loading amount of noble metals or the highly dispersed Pd and Pt species. On the other hand, a peak emerged at $2\theta = 38°$ for Au/CeO_2 and Ag/CeO_2 catalysts which can be identified as (111) diffraction band of face-centered cubic structure Au and Ag. It should be note that all the characteristic peaks of metallic Au and Ag are broad and weak, and the particle sizes calculated through Scherrer equation are all smaller than 3 nm. The *in situ* reduction process has been proved to be effective method for fabrication highly dispersed noble metal nanoparticles on CeO_2 support.

To obtain detailed morphology and noble meal distribution, the materials were examined with transmission electron microscopy (TEM). Fig. 3 shows the TEM results of the meso-structured CeO_2 support and noble metal loaded catalysts. It clearly shows that the meso-structured CeO_2 support was composed by aggregation of nano-crystalline of several nanometers. Pores are randomly but homogeneously distributed within the whole particle, which are produced by a great quantity of gases slowly released from the oxalate precursor leaving behind numerous voids during thermal decomposition process. After impregnation, the noble metal ion species was transferred into the porous structure of CeO_2. The following *in situ* reduction results in noble metal/CeO_2 material with noble metal nanoparticles being homogeneously dispersed in/on the mesoporous support. No large noble metal particle can be found in the TEM images. In addition, the selected area electron diffraction (SAED) patterns from the same area are also presented in the TEM images. The well-defined diffraction rings for CeO_2 can be found in all the samples. However, the relative faint diffraction ring of noble metals may be related to their small loading amount. These results are in good agreement with above XRD analysis.

After loaded with noble metal, the materials still possess mesoporous structure. Impregnation and sequential *in situ* reduction process did not affect the meso-structured nature of the CeO_2 support, as confirmed by the adsorption–desorption isotherms of nitrogen analysis at 77 K (Fig. 4). In all the cases, the typical Langmuir IV isotherms suggest the mesoporous structure and the appearance of H3 hysteresis loops indicate the

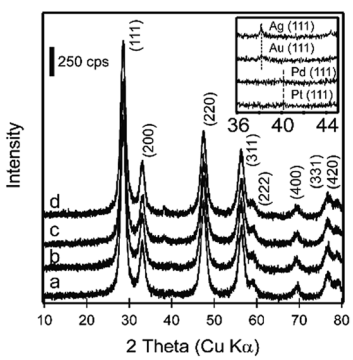

Fig. 2 XRD patterns of 1 wt% noble metal/CeO_2 catalysts: Pd/CeO_2 (a), Pt/CeO_2 (b), Au/CeO_2 (c) and Ag/CeO_2 (d).

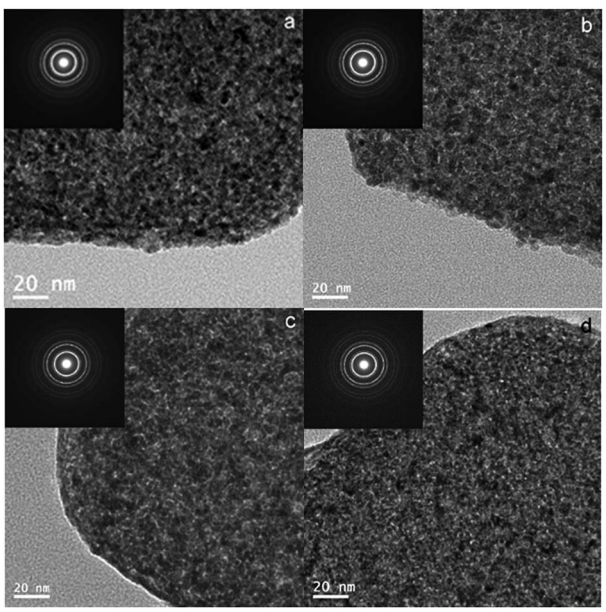

Fig. 3 TEM images and corresponding select area diffraction patterns of 1 wt% noble metal/CeO_2 materials: Pd/CeO_2 (a), Pt/CeO_2 (b), Au/CeO_2 (c) and Ag/CeO_2 (d).

formation of slit-like mesopore. Surprisingly, the specific surface area and pore size of the samples show only limited change after loading of noble metals. These results demonstrate that noble metal nanoparticles have been uniformly dispersed and ungrowth during the deposition process, corresponding well with the above XRD and TEM analysis.

The surface chemical states of the species for noble metal/CeO_2 catalysts were detected by X-ray photoelectron spectroscopy (XPS). Fig. 5A depicts the similar Ce 3d XPS spectra of the different noble metal/CeO_2 catalysts which clearly show the coexistence of Ce(III) and Ce(IV). Generally, the Ce 3d spectrum is somewhat complicated and composed with two series of peaks: $3d_{5/2}$ with two very pronounced "shake-down" satellites and $3d_{3/2}$ with the same characteristic. The satellite peak associated to the Ce $3d_{3/2}$ at 916.9 eV is the characteristic of the presence of tetravalent Ce(IV). The appearance of signals located at about 903.5, 885.4, 898.9 and 880.9 eV, respectively, indicates the existence of Ce(III), which may also use as an indicator for the existence of oxygen vacancies.[20,25–27] The high amount of Ce(III) result in oxygen vacancies which could promote the oxygen release and store and thus directly affect the catalytic performance for HCHO oxidation. The O 1s XPS spectra of the catalysts can be resolved into three peaks as shown in Fig. 5B. The main contribution at 529.1 eV is the characteristic peak of metal–oxygen due to the lattice oxygen (O_{lat}), and that at 530.9 and 532.0 eV are usually associated with the surface chemisorbed oxygen species.[25] In addition, the Pd 3d, Pt 4f, Au 4f and Ag 3d XPS spectrum for the different noble metal/CeO_2 catalysts are also presented in the Fig. 5C–F, respectively.[8,13,14,25] From the corresponding contents of the different noble metal species (ESI†), it can be found that almost all of the noble metal

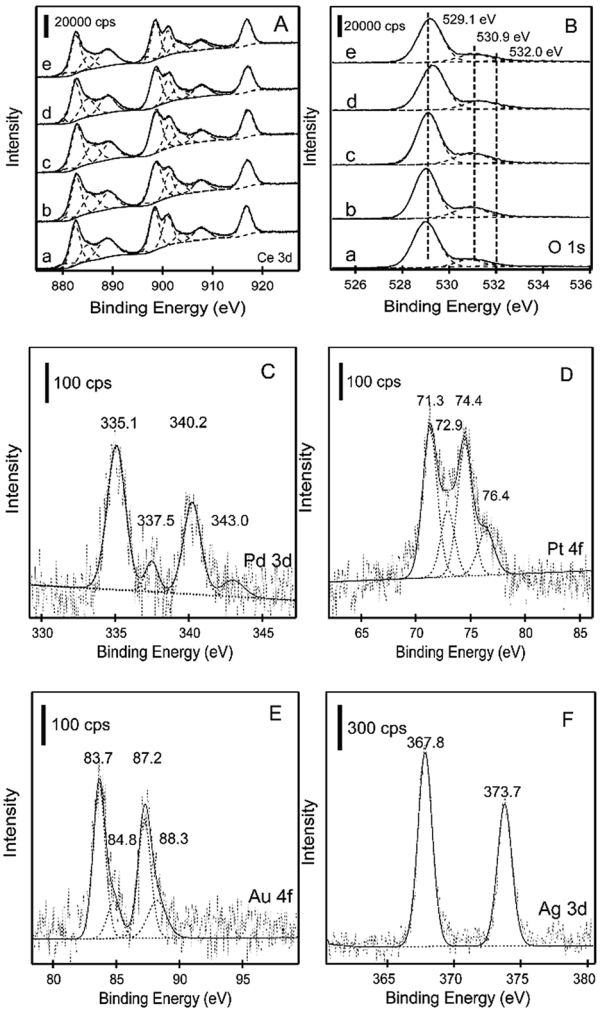

Fig. 5 The XPS spectra of CeO_2 support (a) and noble metal/CeO_2 catalysts. Pd/CeO_2 (b), Pt/CeO_2 (c), Au/CeO_2 (d) and Ag/CeO_2 (e).

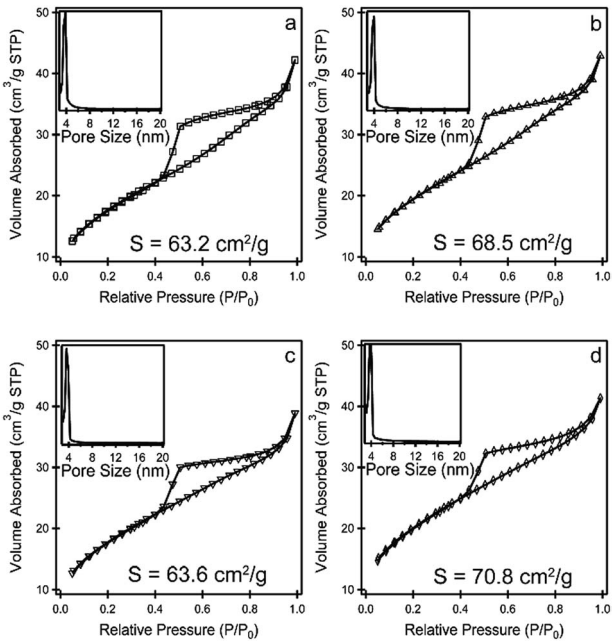

Fig. 4 N_2 desorption–adsorption isotherms and pore distributions of noble metal/CeO_2 materials: Pd/CeO_2 (a), Pt/CeO_2 (b), Au/CeO_2 (c) and Ag/CeO_2 (d).

element exist as metallic in noble metal/CeO_2 catalyst. This may be concerned with the synthesized method in the experiment (post-grafting and reduction).

Fig. 6 shows the similar Raman spectra for the CeO_2 and noble metal loaded CeO_2 samples within 300–600 cm^{-1} range. The main bands centred at about 460 cm^{-1} are typical of CeO_2 vibrations (the triply degenerated TO mode).[28,29] Generally, the intensity of the Raman peaks is related to various parameters of the physicochemical structure of the materials, while the full width at half maximum (FWHM) is associated with the crystallite size and/or the amount of oxygen vacancies.[30,31] In our experiment, the CeO_2 supports are all from the decomposition of the oxalate precursor, and it has been proved that the sequential impregnation and *in situ* reduction process do not affect the crystal size of the CeO_2 support. Thus, a larger FWHM means a high amount of oxygen vacancies in the CeO_2 structure. For noble metal/CeO_2 materials, the FWHM values are all increased when loaded with noble metal, suggesting that the increased concentration of oxygen vacancies. As reported in literature, the oxygen vacancies play a very important role in oxidation reaction process. The high amount of oxygen

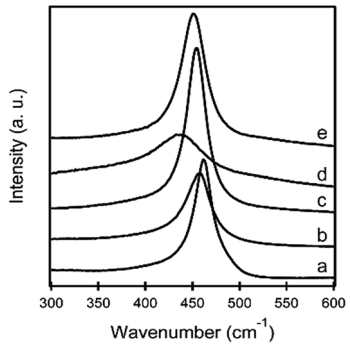

Fig. 6 Raman spectra of CeO_2 support (a) and noble metal/CeO_2 catalysts: Pd/CeO_2 (b), Pt/CeO_2 (c), Au/CeO_2 (d) and Ag/CeO_2 (e).

vacancies may be responsible for the enhanced catalytic activity for HCHO oxidation.

3.3 *In situ* DRIFT study

In situ DRIFT spectra were employed to explain the significantly enhanced catalytic activity of as prepared noble-metal/CeO_2 catalysts solid solution for HCHO oxidation. Fig. 7 shows *in situ* DRIFT spectra of Pd/CeO_2 material exposed to 600 ppm of HCHO + 20.0 vol% O_2 + N_2 at 25 °C. After exposed to HCHO + O_2 + N_2 mixture, the bands at 2940, 2860, 2320, 1540 and 1340 cm^{-1} appeared. With the time increasing, the band intensities increased and reached a steady level after expose for several minutes, more rapid than reported before. According to the literature, two bands at 1540 and 1340 cm^{-1} could be ascribed to ν_{as}(COO) and ν_s(COO). The small bands at about 3050, 2900 cm^{-1} were assigned to ν_s(C–H).[8,11,32] In addition, a weak band appearing at 2320 cm^{-1} is the typical band of CO_2. The immediately emerged and gradually increasing of these spectra suggest that the absorbed HCHO could be rapidly converts to format species intermediates on Pd/CeO_2 catalyst and then decomposed to CO_2. Interestingly, the Pt/CeO_2, Au/CeO_2 and Ag/CeO_2 catalysts showed the similar trend during HCHO oxidation process indicating the almost the same oxidation mechanism.

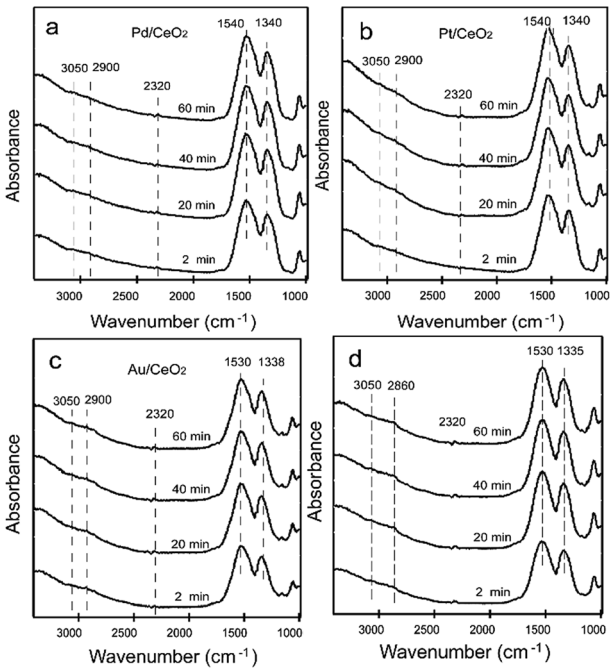

Fig. 7 *In situ* DRIFT spectra of formaldehyde oxidation over noble metal/CeO_2 catalysts: Pd/CeO_2 (a), Pt/CeO_2 (b), Au/CeO_2 (c) and Ag/CeO_2 (d).

3.4 Oxidation mechanism

Why as prepared noble metal/CeO_2 show the much higher catalytic activities for HCHO oxidation? The crystalline structure of the CeO_2 and high dispersing of the active component must be considered. In the present work, the CeO_2 support was fabricated from pyrolysis of oxalate precursor, and resulting meso-structure were composed by aggregation of CeO_2 nanocrystalline which containing much more defect sites and thus provides more oxygen vacancies that are able to absorb and activate O_2, as evidenced experimentally and theoretically. Raman spectroscopies results also reveal that the noble metal loaded CeO_2 catalysts have higher oxygen vacancy concentration compared to the as prepared CeO_2 support, implying a promoting effect of the generation of active oxygen species for the HCHO oxidation reaction. Meanwhile, as can be seen from the TEM and XRD results, the high dispersing of the noble metal may be the other key factor for high catalytic activities for formaldehyde oxidation. Due to the strong synergetic interaction between active component and CeO_2 support, the redox capability of the catalyst is enhanced by the defective CeO_2. Thus, when the catalysts were used in formaldehyde oxidation process, the HCHO could react with the absorbed active oxygen to form COOH intermediates and decomposed to CO_2 rapidly.

4. Conclusions

A series of mesoporous CeO_2 supported noble metal (Pt, Pd, Au and Ag) catalysts were fabricated through a facial pyrolysis and *in situ* reduction protocol and were used for formaldehyde elimination under ambient condition. The as prepared CeO_2 support was composed of the aggregation of CeO_2 nano-crystal with several nanometers, which contain abundant of oxygen vacancies. When combined with noble metal species, the significant catalytic activities could be achieved. For 1% noble metal loaded materials, Pt/CeO_2, Pd/CeO_2 and Au/CeO_2 catalysts could complete catalytic oxidize HCHO at room temperature. Even for the lower-active Ag/CeO_2 catalyst, the complete conversion temperature could be reached to 100 °C, much lower than that reported before. Such highly catalytic properties could be assigned to the strong synergetic interaction between highly dispersed active component and nano-crystalline CeO_2 support with abundant oxygen vacancies.

Acknowledgements

This study was supported by National Basic Research Program of China (973 Program) no. 2013CB933201.

Notes and references

1 T. Salthammer, S. Mentese and R. Matrutzky, *Chem. Rev.*, 2010, **110**, 2536–2572.
2 Y. Sekine, *Atmos. Environ.*, 2002, **36**, 5543–5547.
3 K. J. Lee, N. Shiratori, G. H. Lee, J. Miyawaki, I. Mochida and J. Jang, *Carbon*, 2010, **48**, 4248–4255.
4 Z. Xu, J. Yu and W. Xiao, *Chem.–Eur. J.*, 2013, **19**, 9592–9598.
5 C. Zhang, H. He and K.-I. Tanaka, *Appl. Catal., B*, 2006, **65**, 37–43.
6 C. Zhang, F. Liu, Y. Zhai, H. Ariga, N. Yi, Y. Liu, K. Asakura, M. Flytzani-Stephanopoulos and H. He, *Angew. Chem.*, 2012, **124**, 9766–9770.
7 B. Liu, C. Li, Y. Zhang, Y. Liu, W. Hu, Q. Wang, L. Han and J. Zhang, *Appl. Catal., B*, 2012, **111–112**, 467–475.
8 B.-B. Chen, C. Shi, M. Crocker, Y. Wang and A.-M. Zhu, *Appl. Catal., B*, 2013, **132–133**, 245–255.
9 L. Ma, D. Wang, J. Li, B. Bai, L. Fu and Y. Li, *Appl. Catal., B*, 2014, **148–149**, 36–43.
10 B.-B. Chen, X.-B. Zhu, M. Crocker, Y. Wang and C. Shi, *Appl. Catal., B*, 2014, **154–155**, 73–81.
11 H.-F. Li, N. Zhang, P. Chen, M.-F. Luo and J.-Q. Lu, *Appl. Catal., B*, 2011, **110**, 279–285.
12 R. Averlant, S. Royer, J.-M. Giraudon, J.-P. Bellat, I. Bezverkhyy, G. Weber and J.-F. Lamonier, *ChemCatChem*, 2014, **6**, 152–161.
13 D. Chen, Z. Qu, Y. Sun, K. Gao and Y. Wang, *Appl. Catal., B*, 2013, **142–143**, 838–848.
14 L. Nie, J. Yu, X. Li, B. Cheng, G. Liu and M. Jaroniec, *Environ. Sci. Technol.*, 2013, **47**, 2777–2783.
15 S. Yang, M. Besson and C. Descorme, *Appl. Catal., B*, 2010, **100**, 282–288.
16 H. Huang and D. Y. C. Leung, *ACS Catal.*, 2011, **1**, 348–354.
17 Z. Xu, J. Yu and M. Jaroniec, *Appl. Catal., B*, 2015, **163**, 306–312.
18 S. Song, J. Ding, J. Bao, C. Gao, Z. Qi and C. Li, *Catal. Lett.*, 2010, **137**, 239–246.
19 J. Quiroz Torres, S. Royer, J. P. Bellat, J.-M. Giraudon and J.-F. Lamonier, *ChemSusChem*, 2013, **6**, 578–592.
20 R. V. Gulyaev, E. M. Slavinskaya, S. A. Novopashin, D. V. Smovzh, A. V. Zaikovskii, D. Y. Osadchii, O. A. Bulavchenko, S. V. Korenev and A. I. Boronin, *Appl. Catal., B*, 2014, **147**, 132–143.
21 M.-F. Luo, Z.-Y. Hou, X.-X. Yuan and X.-M. Zheng, *Catal. Lett.*, 1998, **50**, 205–209.
22 B. Wang, D. Weng, X. Wu and R. Ran, *Appl. Surf. Sci.*, 2011, **257**, 3878–3883.
23 A. K. Datye, J. Bravo, T. R. Nelson, P. Atanasova, M. Lyubovsky and L. Pfefferle, *Appl. Catal., A*, 2000, **198**, 179–196.
24 A. S. Ivanova, E. M. Slavinskaya, R. V. Gulyaev, V. I. Zaikovskii, O. A. Stonkus, I. G. Danilova, L. M. Plyasova, I. A. Polukhina and A. I. Boronin, *Appl. Catal., B*, 2010, **97**, 57–71.
25 G. Li, L. Li, Y. Yuan, J. Shi, Y. Yuan, Y. Li, W. Zhao and J. Shi, *Appl. Catal., B*, 2014, **158–159**, 341–347.
26 P. Bera, K. C. Patil, V. Jayaram, G. N. Subbanna and M. S. Hegde, *J. Catal.*, 2000, **196**, 293–301.
27 K. R. Priolkar, P. Bera, M. S. Hegde, S. Emura, R. Kumashiro and N. P. Lalla, *Chem. Mater.*, 2002, **14**, 2120–2128.
28 W. H. Weber, K. C. Hass and J. R. McBride, *Phys. Rev. B: Condens. Matter Mater. Phys.*, 1993, **48**, 178–185.
29 J. M. López, R. Arenal, B. Puértolas, Á. Mayoral, S. H. Taylor, B. Solsona and T. García, *J. Catal.*, 2014, **17**, 167–175.
30 D. Andreeva, R. Nedyalkova, L. Ilieva and M. V. Abrashev, *Appl. Catal., B*, 2004, **52**, 157–165.
31 G. W. Graham, W. H. Weber, C. R. Peters and R. Usmen, *J. Catal.*, 1991, **130**, 310–313.
32 C. Li, K. Domen, K. Maruya and T. Onishi, *J. Catal.*, 1990, **125**, 445–455.